TU/e EINDHOVEN UNIVERSITY OF TECHNOLOGY

Enabling strain imaging in realistic Eulerian ultrasound simulation methods

Citation for published version (APA):
Muller, J-W., Schwab, H-M., Wu, M., Rutten, M. C. M., van Sambeek, M. R. H. M., & Lopata, R. G. P. (2023). Enabling strain imaging in realistic Eulerian ultrasound simulation methods. *Ultrasonics*, *135*, Article 107127. https://doi.org/10.1016/j.ultras.2023.107127

Document license:
CC BY

DOI:
10.1016/j.ultras.2023.107127

Document status and date:
Published: 01/12/2023

Document Version:
Publisher's PDF, also known as Version of Record (includes final page, issue and volume numbers)

Please check the document version of this publication:

• A submitted manuscript is the version of the article upon submission and before peer-review. There can be important differences between the submitted version and the official published version of record. People interested in the research are advised to contact the author for the final version of the publication, or visit the DOI to the publisher's website.
• The final author version and the galley proof are versions of the publication after peer review.
• The final published version features the final layout of the paper including the volume, issue and page numbers.

Link to publication

General rights
Copyright and moral rights for the publications made accessible in the public portal are retained by the authors and/or other copyright owners and it is a condition of accessing publications that users recognise and abide by the legal requirements associated with these rights.

• Users may download and print one copy of any publication from the public portal for the purpose of private study or research.
• You may not further distribute the material or use it for any profit-making activity or commercial gain
• You may freely distribute the URL identifying the publication in the public portal.

If the publication is distributed under the terms of Article 25fa of the Dutch Copyright Act, indicated by the "Taverne" license above, please follow below link for the End User Agreement:

www.tue.nl/taverne

Take down policy
If you believe that this document breaches copyright please contact us at:

openaccess@tue.nl

providing details and we will investigate your claim.

Download date: 17. Nov. 2023

Ultrasonics 135 (2023) 107127

Contents lists available at ScienceDirect

Ultrasonics

journal homepage: www.elsevier.com/locate/ultras

Enabling strain imaging in realistic Eulerian ultrasound simulation methods

Jan-Willem Muller [a,b,*], Hans-Martin Schwab [a], Min Wu [a], Marcel C.M. Rutten [c], Marc R.H.M. van Sambeek [a,b], Richard G.P. Lopata [a]

[a] Photoacoustics & Ultrasound Laboratory Eindhoven (PULS/e), Dept. of Biomedical Engineering, Eindhoven University of Technology, Eindhoven, The Netherlands
[b] Department of Vascular Surgery, Catharina Hospital, Eindhoven, The Netherlands
[c] Cardiovascular Biomechanics Group, Dept. of Biomedical Engineering, Eindhoven University of Technology, Eindhoven, The Netherlands

ARTICLE INFO

Keywords:
Strain imaging
Simulation
Sampling
k-Wave
Cardiovascular

ABSTRACT

Cardiovascular strain imaging is continually improving due to ongoing advances in ultrasound acquisition and data processing techniques. The phantoms used for validation of new methods are often burdensome to make and lack flexibility to vary mechanical and acoustic properties. Simulations of US imaging provide an alternative with the required flexibility and ground truth strain data. However, the current Lagrangian US strain imaging models cannot simulate heterogeneous speed of sound distributions and higher-order scattering, which limits the realism of the simulations. More realistic Eulerian modelling techniques exist but have so far not been used for strain imaging. In this research, a novel sampling scheme was developed based on a band-limited interpolation of the medium, which enables accurate strain simulation in Eulerian methods. The scheme was validated in k-Wave using various numerical phantoms and by a comparison with Field II. The method allows for simulations with a large range in strain values and was accurate with errors smaller than −60 dB. Furthermore, an excellent agreement with the Fourier theory of US scattering was found. The ability to perform simulations with heterogeneous speed of sound distributions was demonstrated using a pulsating artery model. The developed sampling scheme contributes to more realistic strain imaging simulations, in which the effect of heterogenous acoustic properties can be taken into account.

1. Introduction

Ultrasound (US) imaging stands out as medical imaging modality due to its ability to image organs at large depths with a high frame rate. US imaging therefore not only provides spatial information of the tissue scanned, but also allows the analysis of its motion. Many techniques have been described in literature to benefit from this motion information in US, in order to enhance medical diagnostics [1–3]. These techniques include strain elastography and a variety of shear wave elastography methods, such as acoustic radiation force impulse imaging and supersonic shear wave imaging [4–7]. Strain imaging methods currently applied in clinical setting are mainly based on a quasi-static analysis, where the externally applied deformation is relatively small (~1%) [8,9]. Clinical use of quasi-static strain imaging includes grading liver and kidney fibrosis, breast lesion diagnostics, and thyroid and prostate cancer detection. However, the deformation ranges and rates are much larger in cardiovascular tissues, and a quasi-static analysis is therefore not applicable [10]. Furthermore, strain imaging of large cardiovascular organs, e.g., the aorta and the heart, requires sufficient US quality at relatively large depths, which is impeded by speed of sound aberrations, attenuation, and clutter. Therefore, strain imaging for *in vivo* cardiovascular applications remains challenging.

As a result of ongoing advances in beamforming, ultrafast US acquisitions and data processing, cardiovascular image quality is continually improving [11,12]. However, a quantitative *in vivo* evaluation of the benefit of the improved image quality for strain imaging is difficult, due to the lack of a ground truth. Therefore, the use of tissue mimicking phantoms for validation is an important aspect in the development of improved techniques for cardiovascular strain imaging. These phantoms, however, require validation of their properties themselves, are often difficult and time consuming to make, and lack flexibility to vary mechanical and acoustic properties [13]. In contrast, numerical simulations provide an experimental platform in which the phantom properties are exactly known and fully controllable. For these reasons,

* Corresponding author at: P.O. Box 513, 5600 MB Eindhoven, The Netherlands.
E-mail addresses: j.w.muller@tue.nl (J.-W. Muller), h.schwab@tue.nl (H.-M. Schwab), m.wu@tue.nl (M. Wu), m.c.m.rutten@tue.nl (M.C.M. Rutten), marc.v.sambeek@catharinaziekenhuis.nl (M.R.H.M. van Sambeek), r.lopata@tue.nl (R.G.P. Lopata).

https://doi.org/10.1016/j.ultras.2023.107127
Received 28 March 2023; Received in revised form 7 July 2023; Accepted 30 July 2023
Available online 1 August 2023
0041-624X/© 2023 The Author(s). Published by Elsevier B.V. This is an open access article under the CC BY license (http://creativecommons.org/licenses/by/4.0/).

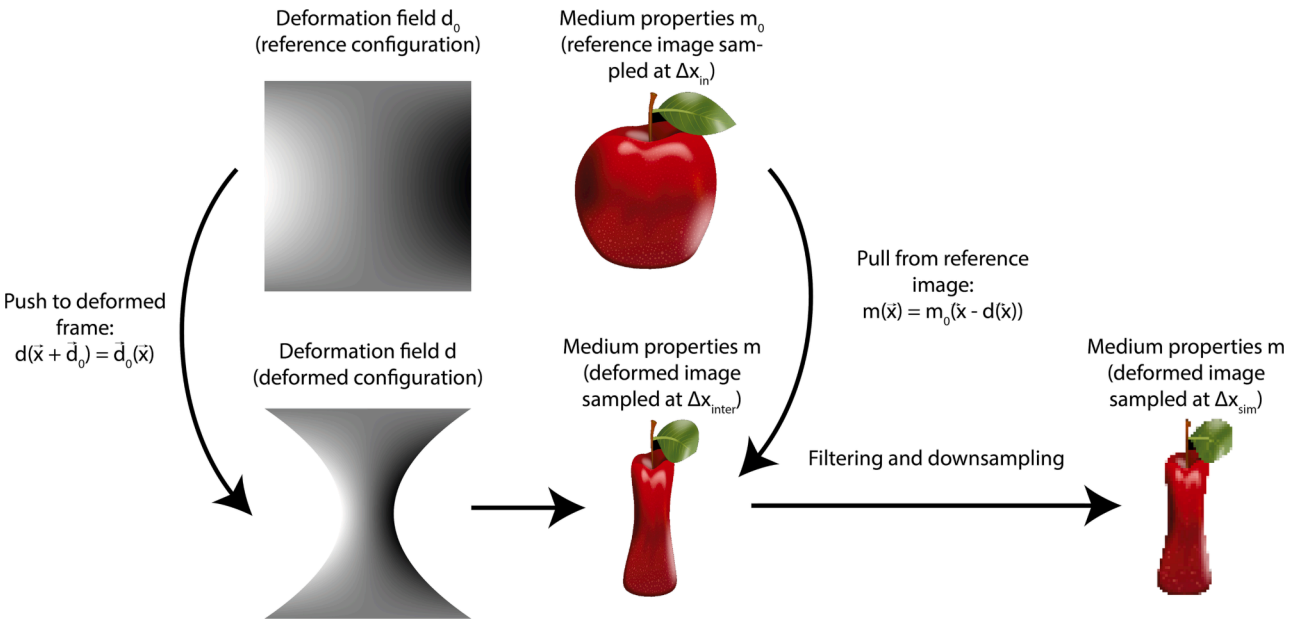

Fig. 1. A schematic overview of the medium displacement method with strain artefact correction. The displacement field $\vec{d}_0$, defined in the reference configuration, is interpolated to the deformed configuration using a push operation. Afterwards, the medium is deformed by interpolating the reference image using a pull approach.

simulations are used to objectively compare the performance of different strain imaging methods [14–16]. Moreover, the controllability of *in silico* experiments can be taken advantage of to generate large datasets of US strain data with a ground truth. Simulations are therefore essential for the development of data-driven methods, for instance machine-learning.

Many US imaging simulation methods and implementations have already been described in literature [17]. The models currently used most often for strain imaging are based on the impulse response method (IRM) [18,19]. In these models, the total acoustic backscatter is calculated by linearly superimposing the received pressure of individual point scatterers. The medium displacement in IRM models is simulated by displacing each point scatterer using a Lagrangian approach. Although the IRM is relatively accurate for simple phantoms, it lacks the ability to simulate complex tissues. For example, heterogeneities in the speed of sound, and higher-order scattering cannot be simulated. These phenomena are the cause of speed of sound aberrations and clutter, which are two major effects that limit the US image quality. Not being able to simulate those phenomena therefore severely limits the realism of strain imaging simulations in complex tissues.

More advanced methods which are capable of simulating most of the relevant physical phenomena by solving the wave equation, have been described in literature [17,20–22]. In these methods, acoustic properties of the simulated medium are prescribed at fixed points in space, which do not move along with the motion of the medium (Eulerian approach). Although Eulerian methods have been shown to be able to realistically simulate US propagation in heterogenous complex media, they have so far not been used for strain imaging.

Therefore, the goal of this study is to develop and analyse the performance of novel sampling methods to enable accurate strain imaging with Eulerian simulation methods. To this end, an interpolation scheme is proposed to accurately resample a deformed medium onto the Eulerian sample points fixed in space. The scheme was specifically designed to be robust against strain induced errors within the medium's spatial frequency bandwidth in the simulation. The scheme is validated using grid-based k-Wave simulations of *in silico* phantoms [22], which were displaced using both homogenous and heterogenous displacement fields. Furthermore, strain imaging results are compared with data obtained from Field II, an IRM often used in literature [23]. Finally, the ability to perform strain simulations in acoustically heterogeneous media is demonstrated with a simulation of a pulsating artery.

2. Methods

2.1. Criteria for the sampling of acoustic properties

Due to the band-limited nature of US signals, an effective interpolation technique for the acoustic property fields can be devised using Fourier theory. According to the Fourier theory of US scattering, a mono-frequent US wave with a wave vector $\vec{k}_{wave}$ interacts uniquely with a specific component in the medium property's frequency space with wave vector $\vec{k}_{medium}$, when neglecting evanescent waves [24,25]. For 180-degree backscatter, the magnitude of $\vec{k}_{medium}$ is the largest: $|\vec{k}_{medium}| = 2\cdot|\vec{k}_{wave}|$. To capture the acoustic behaviour of the medium, it is therefore sufficient to use a bandlimited representation of the medium, with spatial frequencies up to $2\cdot|\vec{k}_{wave}|$. Under deformation, the medium's spatial frequency content changes. It is therefore expected that an accurate simulation of the deformed medium can be performed if all spatial frequencies $\leq 2\cdot|\vec{k}_{wave}|$ are still sampled correctly after deformation. Together with the Nyquist criterion, this implies a sampling of 4 points per wavelength (PPWL) is sufficient. For broadband incoming waves, this criterion refers to the smallest wavelength. From this point of view, a bandlimited interpolant (BLI) is the natural choice for interpolation of the medium [26,27]. An interpolation strategy was developed for deforming bandlimited media sampled on a grid, using the BLI. The details of this strategy are described in Sections 2.2–2.4.

2.2. Displacement of band-limited gridded data

In Eulerian methods, the medium properties in the undeformed configuration, m_0, are described at spatially constant coordinates $\vec{x}$. Motion can be prescribed by deforming m_0 according to a displacement field, to obtain the medium properties in the deformed configuration m. An interpolation is needed to apply the deformation and to resample m on the same Eulerian coordinates. The BLI is most accurate when using

an equidistantly sampled input. Therefore, the undeformed medium properties m_0 are described using a grid. A pull strategy is used, in which m is obtained from the undeformed configuration using a gridded interpolation of m_0:

$$m(\vec{x}) = m_0(\vec{x} - \vec{d}(\vec{x})). \tag{1}$$

where $\vec{d}$ denotes the displacement field in the deformed configuration (how much the medium was moved). The pull approach was implemented using a non-uniform fast Fourier transform (FINUFFT 2.1.0, Flatiron Institute, New York, NY, USA) for fast and efficient interpolation of the undeformed gridded medium properties to their displaced locations using a BLI [28]. In many applications however, the displacement field is defined in the undeformed configuration, $\vec{d}_0$ (how much the medium will be moved). $\vec{d}$ can be obtained by interpolating $\vec{d}_0$ using a push interpolation:

$$\vec{d}\left(\vec{x} + \vec{d}_0\right) = \vec{d}_0(\vec{x}). \tag{2}$$

In this case, a scattered interpolation is needed to resample the scattered data, pushed to the displaced location $\vec{x} + \vec{d}_0$, onto the Eulerian coordinates $\vec{x}$. For an overview of all interpolation steps, see Fig. 1.

2.3. Strain artefact reduction

For homogeneous displacement fields, the effective strain is zero, and the BLI can be used for interpolation without complications. However, an inhomogeneous displacement field will result in non-zero strains and causes two artefacts for band-limited interpolation. 1) For positive strain values, the maximum spatial frequency present in the medium is decreased. This effect can affect the simulated interaction between the US wave and the medium at high frequencies. 2) For negative strain values, compression will occur. This compression increases the maximum spatial frequency present in the sampled medium, which can lead to aliasing if the sampling spacing is not sufficient. In this study, we propose a sampling scheme that is robust against these strain-induced artefacts.

The input medium is prescribed in the undeformed state. In case of a positive strain, the effective maximum frequency in the medium is decreased after deformation. The largest frequency in the medium may not drop below the maximum supported frequency in the simulation, after deformation. Therefore, the sampling spacing of the input medium Δx_{in} must be smaller than the spacing of the simulation grid Δx_{sim}:

$$\Delta x_{in} = \frac{\Delta x_{sim}}{1 + \epsilon}, \tag{3}$$

where ϵ is the global maximum nominal strain [29]. In case of a negative strain, aliasing will occur if the deformed medium is sampled with the same spacing as the undeformed input medium. Therefore, the deformed medium is first sampled on an intermediate grid with a spacing Δx_{inter}, which is smaller than Δx_{in}. Due to the compression of the medium, the medium's maximum spatial frequency in the intermediate grid is increased. Consequently, a low-pass filter is needed to remove frequencies larger than $\frac{1}{2\cdot\Delta x_{sim}}$, as these cannot be sampled correctly with the grid used in the simulation. After filtering, down-sampling is applied to obtain a spacing of Δx_{sim} for use in the simulation. The largest value of Δx_{inter} for which no harmful aliasing is present, can be derived analytically. The alias frequency k_{alias} for the highest frequency present in the medium after deformation, k_{deform}, can be expressed as:

$$k_{alias} = \frac{1}{\Delta x_{inter}} - k_{deform}, \tag{4}$$

$$k_{deform} = \frac{1}{2\cdot(1-c)\cdot\Delta x_{in}}, \tag{5}$$

where c is the absolute value of the global minimum nominal strain [29]. Aliasing is allowed for frequencies larger than $\frac{1}{2\cdot\Delta x_{sim}}$, as these frequencies are filtered out by the low-pass filter afterwards. Therefore, to obtain the optimal (largest) value of Δx_{inter}, k_{alias} is set equal to $\frac{1}{2\cdot\Delta x_{sim}}$. Together with Eq. (4) and Eq. (5), this results in:

$$\Delta x_{inter} = \frac{1}{\frac{1}{2\cdot\Delta x_{sim}} + \frac{1}{2\cdot(1-c)\cdot\Delta x_{in}}} = \frac{2\cdot(1-c)\cdot\Delta x_{in}\cdot\Delta x_{sim}}{(1-c)\cdot\Delta x_{in} + \Delta x_{sim}}. \tag{6}$$

By substituting Eq. (3) into Eq. (6), Δx_{inter} can be determined for heterogenous strain fields, when both positive and negative strains are present:

$$\Delta x_{inter} = \frac{2\cdot(1-c)}{2 + \epsilon - c}\cdot\Delta x_{sim}. \tag{7}$$

Note that in 2D and 3D, ϵ and c denote the global maximum principal strain and the absolute value of the global minimum principal strain respectively. If multiple deformed states are simulated, ϵ and c are always defined with respect to the undeformed state (cumulative strain values).

2.4. Eulerian and Lagrangian backscatter intensities

The sampling strategy proposed was designed to interpolate the frequency content of the undeformed medium correctly using a BLI. However, applying strain to a medium not only induces a change in appearance, but also affects the intensity of the received simulated backscatter. The relation between strain and backscatter intensity is different between the Eulerian approach proposed in this study, and the IRM employing a Lagrangian approach. In the IRM, fully developed speckle can be generated by superimposing the received pressure signals of many (> 10 per resolution cell) randomly positioned point scatterers [23]. For fully developed speckle, the acoustic intensity (I_L) is proportional to the scatterers' number density (ρ_N). The relative number density will vary according to the local strain value, and will thereby affect the speckle intensity:

$$I_L \propto \rho_N \propto \frac{1}{1 + \Delta V}, \tag{8}$$

where ΔV denotes the local volumetric strain. In a Eulerian approach, white noise speckle may be generated by adding a Gaussian variation to the medium property fields. The BLI conserves the signal amplitude while interpolating m_0, but as a consequence, does not conserve signal energy under strain. Straining the signals in m_0 with constant amplitude, results in an additional scaling of the medium's energy spectral density (S) with $(1 + \Delta V)^2$. As the speckle intensity in the Eulerian approach, I_E is proportional to S (for small impedance variations) [25], strain will influence the speckle intensity according to:

$$I_E \propto S \propto (1 + \Delta V)^2 \cdot I_L \propto 1 + \Delta V. \tag{9}$$

Eq. (8) and Eq. (9) were used pragmatically in this study to quantitatively compare speckle from simulations using the two different approaches, see Section 2.7. Note that the scaling of both I_L and I_E with respect to $(1 + \Delta V)$, as derived here, are only valid for a white noise model to generate speckle. The ratio between I_E and I_L, $(1 + \Delta V)^2$, however, is caused by the BLI and therefore independent of the speckle model used. Although the white noise model allows for a straightforward comparison between the Lagrangian and Eulerian approach, it may not be a realistic model for all media. For a physically correct and quantitative simulation, the behaviour of each medium property (e.g. density, speed of sound or point scatterer's amplitude) should be modelled as function of strain individually. However, the quantitative simulation of speckle under strain is outside the scope of this study.

Table 1
A summary of all simulations performed, briefly stating the purpose and simulation settings used.

Simulation Description	Purpose	Settings
1D homogeneous displacement simulation (Section 2.6)	Characterizing errors of several interpolation methods for medium displacement	Δx_{sim}: 25 μm.
2D simulation with uniaxial strain (Section 2.7)	Analyzing strain simulation performance in a controlled way using a reference simulation	Δx_{sim}: 29.6 μm Acquisition: single plane wave
2D simulation of incompressible medium with heterogeneous strain (Section 2.8)	Comparing strain results with Field II, using a finite element model of a compressed medium	Δx_{sim}: 25 μm Acquisition: 13 coherent plane waves
2D strain simulation of an artery with speed of sound aberration (Section 2.9)	Verifying the ability to simulate strain imaging in acoustically heterogeneous tissues	Δx_{sim}: 25 μm Acquisition: 13 coherent plane waves

2.5. Experimental set-up

To investigate the performance of the methods proposed for deforming gridded media, several numerical experiments were performed with k-Wave [22] using Matlab (R2022b, The Mathworks, Natick, Massachusetts, USA). The details of these experiments are described in the Sections 2.6–2.9 hereafter but are also summarized in Table 1 for reference. In all experiments in this study, a Verasonics (Kirkland, Washington, USA) L11-5v linear array transducer was simulated. The transducer consisted of 128 elements with a pitch of 300 μm and an element width of 270 μm. The center frequency was 7.6 MHz and the channel data were sampled with a frequency of 31.25 MHz. The bandwidth of the probe was 75% (at −6 dB), unless stated otherwise. The frequency response of the probe was simulated using a Hann window in the temporal Fourier domain. For further details on the implementation of the transducer properties in k-Wave, the reader is referred to [27].

2.6. Error analysis of homogenous medium displacement

Interpolation of the medium may introduce errors in both the amplitude and the phase of received backscatter. The introduced errors were compared for several interpolation methods (linear, cubic, spline and BLI) while applying homogeneous medium displacement in a 1D k-Wave simulation. Δx_{sim} was set to 25 μm, corresponding to ~7.9 PPWL at the centre frequency. An echoic region with a diameter of 2 mm (~10λ) was simulated at a depth of 1 cm within an anechoic background medium with a density of 1000 kg/m^3 and a speed of sound of 1500 m/s. The echoic region was simulated by adding random Gaussian fluctuations to the density or the speed of sound map. Two different types of simulations were performed: 1) The Gaussian fluctuations were added to the density map, and the speed of sound remained constant and 2), the fluctuations were added to the speed of sound map, and the density map remained constant. The standard deviations of the distributions were 1 kg/m^3 and 1 m/s respectively. Sub-pixel displacements, between 0 and Δx_{sim}, were applied to the medium. In this 1D simulation, the point spread function is independent of the spatial location. Therefore, the displacement of the medium should not alter the received backscatter signal apart from the time-of-flight. To compare the results of the displaced medium with those of the reference simulation, the received channel data were corrected for the altered time-of-arrival. The pressure signals were shifted in time using a BLI, for which the bulk speed of sound was used to determine time offset caused by the medium displacement. After correction, the resulting channel data were compared using the root-mean-square (RMS) pressure and average phase of the backscatter to analyse the performance of the different interpolation methods.

2.7. Error analysis of heterogenous medium displacement

The accuracy of the Eulerian BLI sampling strategy to simulate strained media was determined using a 2D k-Wave simulation. To obtain a reference to compare with, the medium was described using a Lagrangian approach. Each point scatterer was defined off-grid and sampled on the k-Wave grid using a BLI. In the Eulerian displacement approach, the displacements were applied after sampling the point scatterers, using the scheme proposed. In the Lagrangian displacement approach, the point scatterers were moved according to the displacement field first, before being sampling on the grid. Although the Lagrangian approach is limited to media defined by point scatters only, it provides an accurate reference to compare with, while the proposed Eulerian method can be applied to any gridded medium definition. An echoic disc with a diameter of 2 mm (~10λ) was simulated at a depth of 1 cm within an anechoic background medium with a bulk density of 1000 kg/m^3 and a bulk speed of sound of 1500 m/s. The echoic region was simulated using 10^4 point scatterers (~3200 scatters per mm^2) placed randomly within the disc with a uniform spatial distribution, to create fully developed speckle. The amplitude of the point scatterers was sampled from a Gaussian distribution with a standard deviation of either 1 kg/m^3 or 1 m/s, and the resulting fields were added to the bulk density and bulk speed of sound fields respectively. The channel data were simulated for multiple axial strain values, whereas the lateral displacement was set to zero. The axial displacements were chosen to be linearly increasing with axial position, relative to an offset O_{ax}. This results in an analytical description of the displacement fields as:

$$d_{0ax}(x_{ax}) = \epsilon_{ax} \cdot (x_{ax} - O_{ax}), \tag{10}$$

$$d_{ax}(x_{ax}) = \frac{\epsilon_{ax} \cdot (x_{ax} - O_{ax})}{1 + \epsilon_{ax}}, \tag{11}$$

where d_{oax}, d_{ax}, x_{ax} and ϵ_{ax} denote the axial displacement in the reference frame, the axial displacement in the displaced frame, the axial Eulerian position and the axial strain respectively. O_{ax} is the origin of the axial strain, where the displacement and strain are zero, and was set to a depth of 1 cm. The strains ranged from −0.5 to 0.5 and were each applied to the undeformed medium in a single deformation step. In the Eulerian approach, ϵ and c were both set to either 0, for no strain artefact corrections, or both to a value of 0.1. The relative scattering amplitude of the field was multiplied by $\sqrt{1+\epsilon_{ax}}$ in the Lagrangian approach, and by $\frac{1}{\sqrt{1+\epsilon_{ax}}}$ in the Eulerian approach, to ensure strain independent speckle intensities in the received channel data in both approaches. US simulations were performed using a single 0 angle plane wave, which allowed for a straightforward comparison of the strain induced errors with the Fourier theory of scattering. The delay-and-sum (DAS) beamformed RF images were compared to the DAS beamformed images obtained with the reference method to determine the performance of the strain method proposed. The error in dB was determined in a circular region of interest with a radius of 3 mm around the inclusion, according to:

$$\varepsilon = 10 \cdot \log_{10} \frac{\sum (p - p_{ref})^2}{\sum p_{ref}^2}. \tag{12}$$

The sampling scheme proposed was designed to correctly sample all frequencies in the k-Wave grid after deformation with a strain value in the range $[-c, \epsilon]$. However, if the k-Wave grid is sampled with more than 4 PPWL of the maximum US pulse frequency, a part of the highest spatial frequencies in the medium has no interaction with the US pulse, see Section 2.1. This implies the scheme proposed may still be accurate even for strains outside the range $[-c, \epsilon]$, if the undeformed grid is sampled with more than 4 PPWL. To analyse the influence of the maximum frequency of the transmitted pulse on the accuracy of the sampling scheme, two different bandwidths were used. Simulations were performed with bandwidths of 37.5% and 75% (at −6 dB), both with a Δx_{sim} of 29.6 μm.

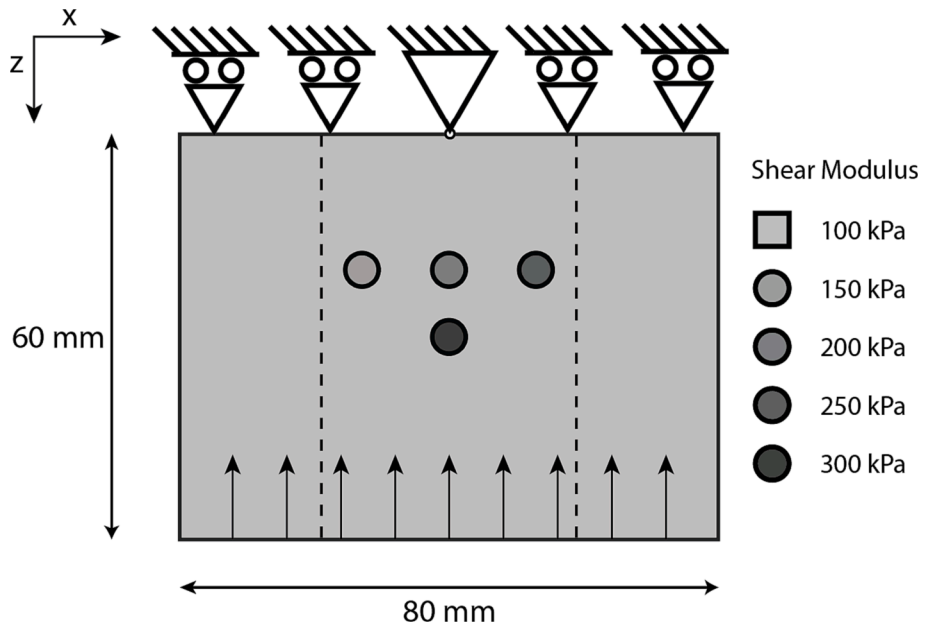

Fig. 2. An *in silico* strain phantom with four stiffer inclusions, which was imaged using a linear array. The bottom face of the phantom was displaced towards the top, causing a bulk strain of 5%. The top face was only constrained in z-direction. The aperture of the probe is indicated with the dotted lines.

This specific value corresponds to exactly 4 PPWL of the maximum frequency present in the 75% bandwidth pulse (12.7 MHz, at −60 dB) and therefore corresponds to the coarsest sampling possible according to the Fourier theory of US, see Section 2.1. The maximum frequency present (-60 dB) in the 37.5% bandwidth pulse was 10.1 MHz (5 PPWL) and is therefore sampled finer than theoretically needed.

2.8. Strain imaging comparison between k-Wave and Field II

The quality of the strain simulations using the sampling scheme proposed was further analysed in a more realistic use case. The compression of a 2D soft tissue phantom was simulated in both k-Wave and Field II [22,30]. Field II was chosen to provide a reference simulation, as it has a been used extensively in literature to simulate motion in media with a homogenous speed of sound [17,18]. The centre of the simulated US array was used as the origin of the coordinate system. The phantom contained four inclusions with a diameter of 5 mm, placed at a depth of 20 and 30 mm, see Fig. 2. The bulk tissue's shear modulus was 100 kPa, and the four inclusions had an increasing shear modulus between 150 and 300 kPa. The displacements in the tissue were obtained using a finite element simulation, using a plane strain incompressible Neo Hookean model in Abaqus (2019, Dassault Systèmes, Vélizy-Villacoublay, France), with triangular CPE6H elements. The mesh was obtained using Triangle 1.6 [31], and refined with MMG (5.6.0, INRIA,

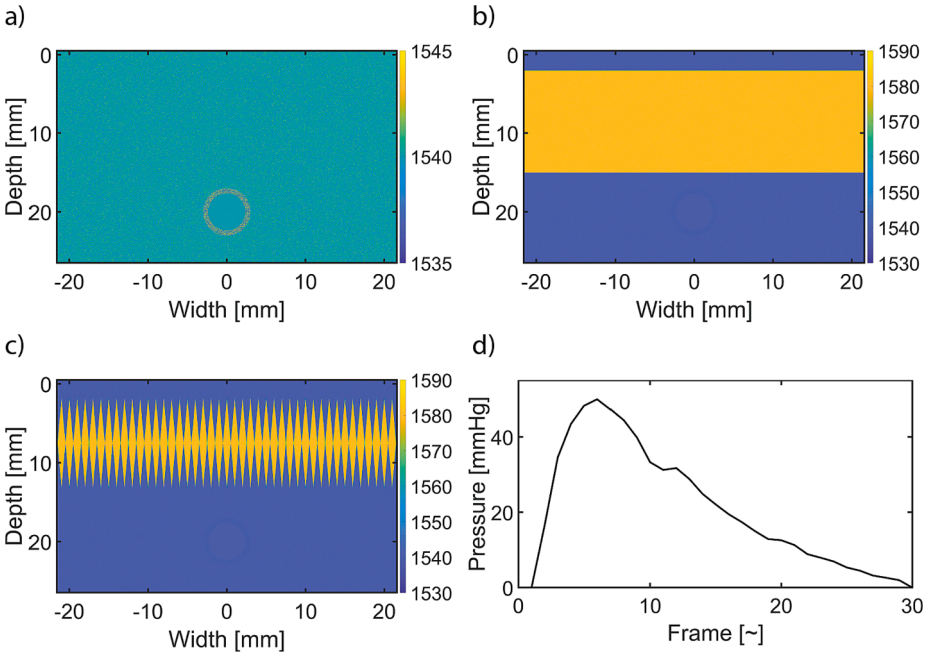

Fig. 3. (a–c) The homogeneous, layered, and aberrating speed of sound maps used in the pulsating artery simulations are shown respectively. Note that the speed of sound is identical inside the vessel for all media. (d) The pressure applied to the inner wall of the artery as function of the frame number.

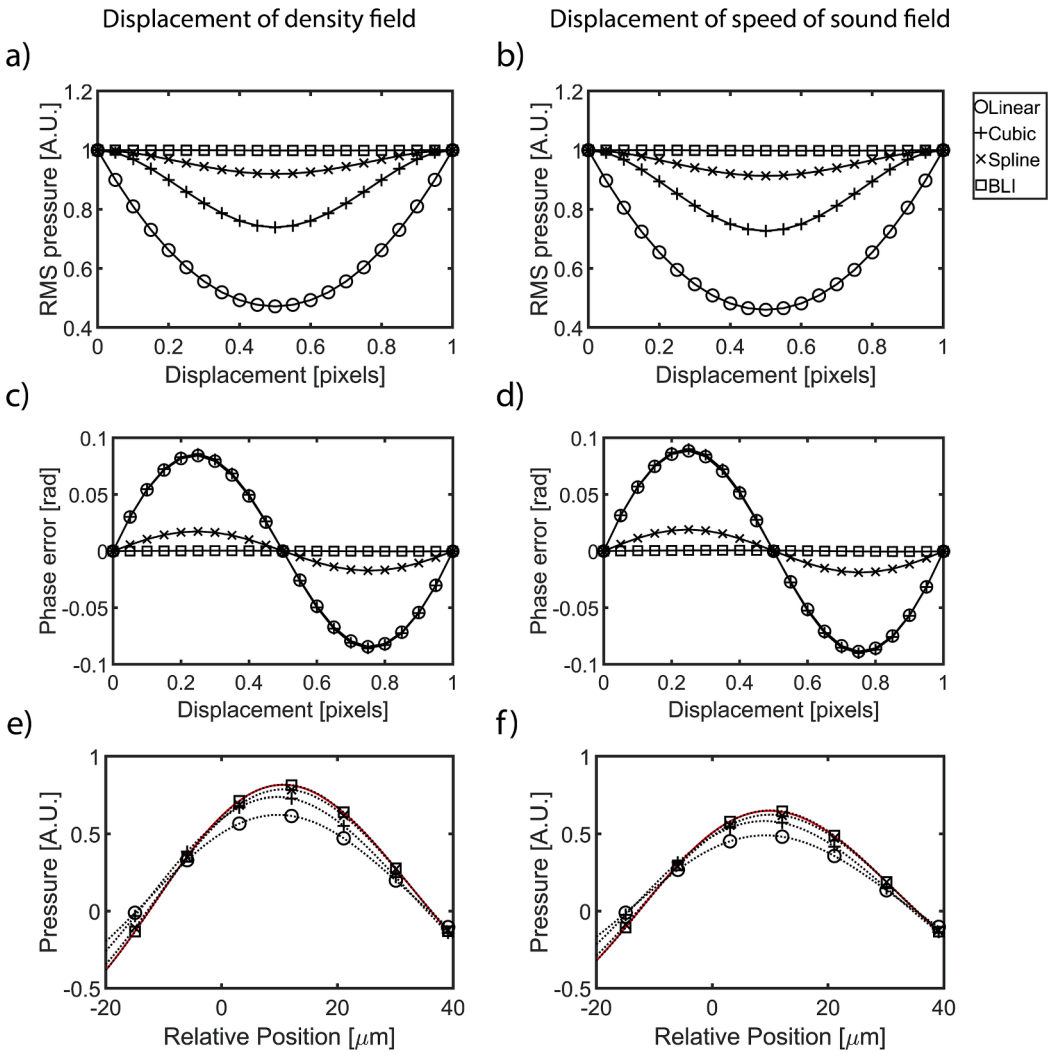

Fig. 4. The performance of different interpolation methods for homogenous displacement in 1D is shown. (a, b) The RMS pressure for sub-pixel displacements of the density field and speed of sound field. (c, d) The phase error for sub-pixel displacements of the density field and speed of sound field. (e, f) Time of flight corrected reconstruction of the pressure with a medium displacement of 0.25 pixels. The solid red line shows the pressure for the zero-displacement reference simulation. The position is relative to the center of the echoic region.

Bordeaux, France), with a target maximum edge length of 1 mm for the bulk tissue and 0.1 mm for the inclusions. Compression was applied by prescribing the displacements in the z-direction at the bottom face of the phantom. The motion at the top face was restricted in z-direction but allowed to move in x-direction. A bulk compression of 5% was prescribed in steps of 0.5%, yielding 11 frames with displacement data. The mean lateral displacement in each frame was subtracted from the displacements, to ensure that no global lateral drift occurred. The nodal displacement values in the deformed frame were interpolated to a Eulerian grid using a linear interpolation in each triangular element. For each frame, 13 plane waves with angles between -15 and $+15$ degrees were compounded to obtain 11 US images. In k-Wave, the channel data were generated in 2D using a Δx_{sim} of 25 μm. The displacement was applied using the sampling scheme proposed, in which both ϵ and c were set to 0.07. Speckle was generated with uniform spatial intensity by adding Gaussian noise to the input density map.

In Field II, the channel data was generated using a sampling frequency of 100 MHz, which was down sampled to 31.25 MHz using a BLI. Speckle was generated by randomly placing scatterers in the 2D imaging plane with Gaussian distributed amplitudes. Out-of-plane scatterers were not simulated, consistent with the 2D geometry simulated in k-Wave. The impulse response in Field II, however, propagates as a 3D spherical wave, whereas in the 2D k-Wave simulation it is cylindrical. This leads to minor received pressure amplitude differences between the methods as function of depth, but its effect is deemed negligible for the speckle's local properties in the US images. The spatial density of the scatterers was 500 mm^{-2}, which was found to be sufficient to generate fully developed speckle. The channel data were DAS beamformed on a Cartesian grid and demodulated to baseband IQ data.

The displacements in both simulations methods were estimated on a new Cartesian grid, using a block-matching method, employing the normalized cross-correlation. The axial and lateral displacement kernel sizes were 21 by 29 pixels (1050 μm by 1450 μm). Afterwards, strain values were calculated using a least-squares strain estimator (LSQSE), with a kernel size of 11 by 11 pixels (2750 μm by 2750 μm) [32]. The reference strain field obtained from the FEM simulations was determined using the same LSQSE, to eliminate effects of the strain estimation method itself. The strain fields were compared using the elastographic signal-to-noise ratio SNR_e:

$$SNR_e = 20 \cdot \log_{10}\left(\frac{|\mu_{inc}|}{\sigma_{back}}\right)$$

where μ_{inc} denotes the cumulative mean axial strain in the inclusions, and σ_{back} the standard deviation of the cumulative background axial strain.

2.9. Pulsating artery in acoustically heterogeneous media

The ability to perform strain imaging in acoustically heterogeneous media was verified using a simulation of a pulsating artery. The artery was rotationally symmetric and had an outer radius of 3 mm and a wall thickness of 0.65 mm. The motion of the artery was modelled using an

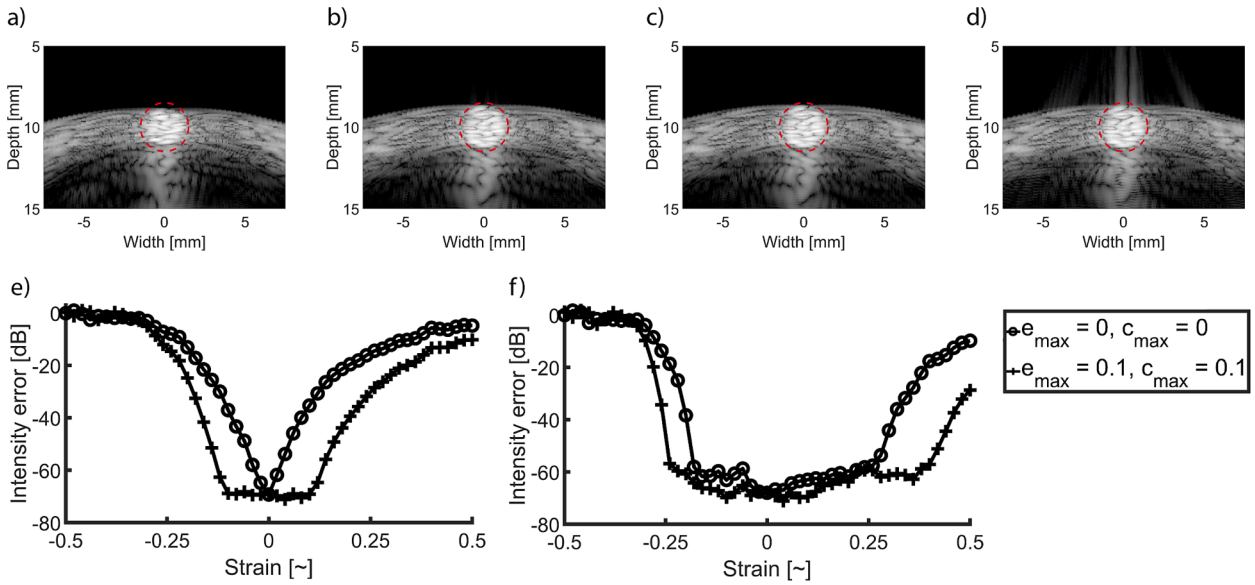

Fig. 5. The reconstructed B-mode images (60 dB dynamic range, 75% bandwidth) of the strained 2D disk are shown for different sampling strategies of the density map: (a) Undeformed reference; (b) 20% strain using the BLI with the sampling method proposed; (c) 20% strain using the reference method; (d) 20% strain using the BLI without strain correction. The intensity error as function of strain is shown for the 37.5% and 75% bandwidth simulations in (e) and (f) respectively.

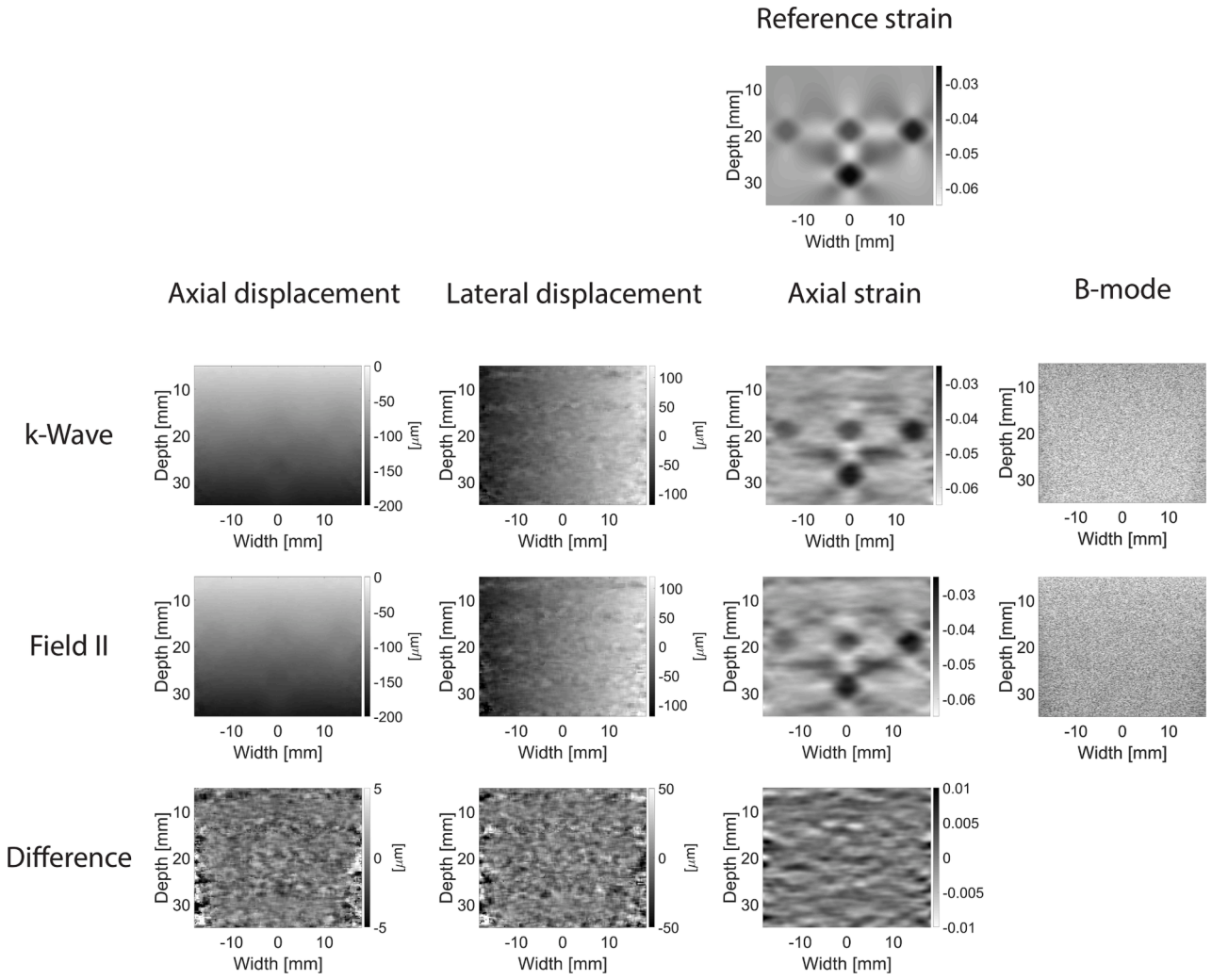

Fig. 6. The displacement tracking (frame 10 to 11), cumulative strain (frame 11) and B-mode (frame 11, 60 dB dynamic range) imaging results are shown for both the Field II simulation and the k-Wave simulation with the sampling method proposed.

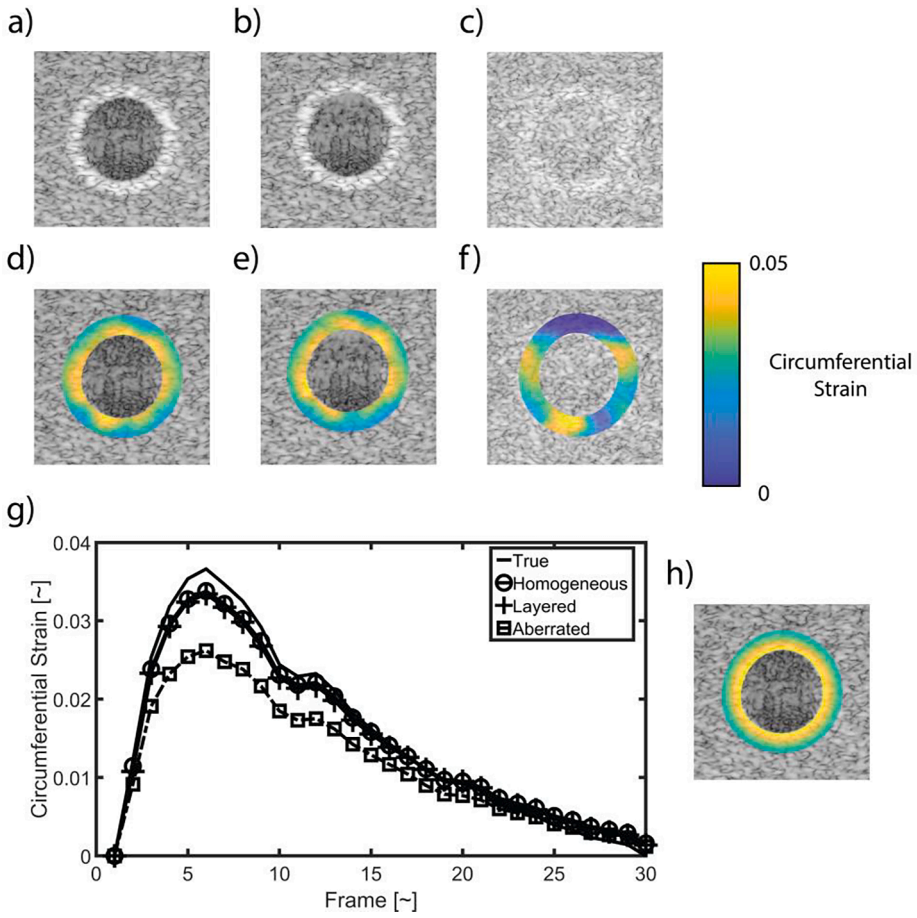

Fig. 7. The results of the pulsating artery simulation in the three different acoustic media are shown. (a–c) The B-mode images (frame 6, 60 dB dynamic range) are shown for the heterogenous, layered and aberrated medium respectively. (d–f) The circumferential strain overlayed over the B-mode image at peak systole (frame 6) are shown in the heterogenous, layered and aberrated medium respectively. (g) The global median circumferential strain as function of frame number is shown. (h) The reference true strains overlayed over the homogeneous medium B-mode image at peak systole (frame 6).

analytical incompressible plane strain model, in which the Young's modulus was set to 500 kPa [33]. A pressure pulse was applied on the inner wall of the vessel in 30 frames, see Fig. 3(d). For each frame, 13 plane waves with angles between −15 and +15 degrees were simulated (as in Section 2.8) and compounded to obtain 30 US images. The artery was embedded in three media with a different speed of sound distribution: 1) a homogeneous speed of sound of 1540 m/s, 2) a 17 mm flat layer with a speed of sound of 1580 m/s within a background speed of sound of 1540 m/s and 3) an aberrating layer with a speed of sound of 1580 m/s within a background speed of sound of 1540 m/s, see Fig. 3 (a)–3(c). In all cases, the density was set to a constant value of 1000 kg/m^3. To add speckle, Gaussian noise with a standard deviation of 1.35 m/s and 4.28 m/s was added to the bulk speed of sound map, in the background and artery wall respectively. No speckle was added in the lumen. The parameters ϵ and c were both set to 0.07, which was sufficient for the absolute maximum analytical strain of ~0.05 at peak systole. Displacement tracking and strain imaging were performed with identical parameters as described in Section 2.8, apart from the size of the strain kernel. Here, the size of the strain kernel was 3 by 5 pixels (600 μm by 2400 μm) in radial and circumferential direction respectively.

3. Results

3.1. Error analysis of homogenous medium displacement

Simulations of an echoic region were performed in 1D, to analyse the performance of various interpolation methods when applying homogeneous displacements to the medium, see Fig. 4. The RMS pressure of the received backscatter is dependent on both the displacement, measured as fraction of a pixel in the k-Wave grid, and the interpolation method used. The linear interpolation method performed worst. It resulted in an RMS pressure of 47% and 46% with respect to the reference RMS pressure, when interpolating the density and speed of sound map respectively, see Fig. 4(a) and 4(b). Although cubic and spline interpolation show a smaller RMS pressure underestimation, only the BLI method is capable of displacing both medium properties without significantly affecting the RMS pressure. The phase errors of the received signals show a similar behaviour, see Fig. 4(c) and 4(d). Again, linear interpolation performed worst, now together with cubic interpolation, and the BLI shows no significant phase errors. The phase errors were similar when displacing the density map and the speed of sound map, for all interpolation methods. Overall, the absolute phase errors were relatively small for all interpolation methods, with a maximum absolute error of 0.09 rad.

3.2. Error analysis of heterogenous medium displacement

An analysis of the performance of the sampling method proposed was performed using 2D simulations of a strained echoic disc region. Oscillations in the RF data are introduced when strain is applied to the speed of sound or density map using the BLI without corrections ($\epsilon = c = 0$). These oscillations can be observed in the envelope detected B-mode images as white streaks in the background but are not visibly present in the region within the discs, see Fig. 5(d). With the proposed sampling scheme, these distortions can no longer be observed in the image after deformation, see Fig. 5(b). To analyse the improvement quantitatively, the beamformed RF data were compared with the data obtained from reference simulations (Lagrangian displacement of the scatterers). The mean relative error was determined using Eq. (12). A circular region with a diameter of 3 mm around the discs after deformation was used as region of interest, see Fig. 5. For the 75% bandwidth pulse, the medium

was sampled at the theoretical lower limit, with exactly 4 PPWL at 12.7 MHz (maximum frequency present). Therefore, it is expected that any non-zero strain will lead to increased intensity error if no corrections are applied. This was also observed experimentally, e.g., the error increased from around −70 dB at zero strain, to −37 dB for −0.1 strain and to −35 dB for 0.1 strain. When strain corrections were applied with the method proposed ($\epsilon = c = 0.1$), the error remained relatively stable at a value of −70 dB for strain values between −0.1 and 0.1, in accordance with the prescribed values for c and ϵ. The intensity error of the data simulated with a 37.5% bandwidth pulse shows a different behaviour as function of strain, see Fig. 5(f). In this case, the sampling of the medium was 5 PPWL at 10.1 MHz (maximum frequency), smaller than the theoretical limit of 4 PPWL. The theoretically calculated range of strain values for which the spatial frequencies smaller than $\frac{1}{4\lambda}$ (at 10.1 MHz) are still sampled correctly, were determined using Eq. (3) to Eq. (5). These ranges were −0.17 to 0.25 and −0.23 to 0.37, for the uncorrected and corrected data, respectively. This agrees well with the experimental results, as within these ranges the intensity error remained smaller than approximately −60 dB. Still, a slight increase in error within the ranges is observed for larger absolute strain values. However, for strain values outside the theoretically calculated ranges, the error increases much faster in both directions. For these larger absolute strain values, the spatial frequencies in the medium smaller than $\frac{1}{4\lambda}$ are no longer sampled correctly. Consequently, the interaction between the medium and the high frequencies pressure waves in the US pulse is affected. Note that the results discussed here were obtained from simulation in which the density map was deformed. The intensity errors in simulations in which the speed of sound map was deformed, show an almost identical behaviour, see Fig. A1.

3.3. Strain imaging comparison between k-Wave and Field II

Strain imaging of a tissue phantom with four stiffer inclusions was simulated. The results obtained using k-Wave, with the correction method proposed, were compared to the reference method employing field II, see Fig. 6. Overall, the estimated displacement fields are very similar between the k-Wave and Field II, both in axial and lateral direction. The estimated cumulative axial strain fields, after displacement tracking of the 11 frames, are almost identical in appearance. Both displacement fields and the axial strain could be determined accurately with the k-Wave data, as no bias compared to the Field II results is observed. Furthermore, the irregularities in the background, caused by an imperfect displacement tracking, are comparable in amplitude. The mean and standard deviation of the SNR_e for the inclusions were 21.2 ± 1.2 dB using Field II, and 22.1 ± 1.2 dB using k-Wave.

3.4. Pulsating artery in acoustically heterogeneous media

Strain imaging simulations were of a pulsating artery were performed in three different acoustic media, see Fig. 7. The circumferential strains in the artery could be determined relatively accurately in the simulations with the homogeneous and layered speed of sound media. In both cases, the circumferential strain shows the expected spatial distribution, where the magnitude of the strain is highest for smaller radii. The larger speed of sound in the layered medium caused the apparent position of the vessel to shift upwards. Furthermore, the layer had a defocussing effect and slightly worsened the contrast of the lumen, compared to the homogeneous speed of sound medium. Still, these effects only had a minor influence on the determined spatial strain distribution and median strain curve over time. In the aberrating medium, however, the decrease in contrast was more severe, and the determined spatial distribution of the strain was worse. The regions at the top and bottom, where the circumferential direction corresponds to the lateral direction of the US beam, were affected more by the aberration. The median strain curve over time showed a more severe underestimation of the strain, compared to the homogeneous and layered media results.

4. Discussion

Simulations of US strain imaging have been used extensively in literature for both the development and the validation of novel strain imaging techniques. The models currently used describe the tissue properties as a collection of moving point scatterers using the IRM. The IRM lacks realism, as the effects of speed of sound aberrations and clutter are not modelled. More advanced and realistic Eulerian US wave propagation models exist, which sample the tissue at fixed points in space. In this study, a sampling scheme was developed and validated using k-Wave, which enables the simulation of tissue motion and deformation in Eulerian methods. The developed methods allow for simulations of strain imaging in which effects of aberration and refraction are included.

The scheme proposed was developed by means of a Fourier-based description of US scattering in heterogeneous media. As expected from this theory, the BLI was the most accurate method to displace scattering tissue, as compared to linear, cubic and spline interpolation. Although the phase errors remained relatively small, the amplitude of the reflected waves were underestimated for all interpolation methods other than the BLI. The underestimation of the amplitude depends on the type of interpolation and the displacement but was as high as 54% for the linear interpolation method. This implies that for heterogeneous displacement fields, erroneous decorrelation of speckle may occur, as not all reflections are underestimated by the same amount. Furthermore, some displacement estimation methods are particularly sensitive to the amplitude of the received backscatter, such as optical flow tracking. Therefore, the BLI increases accuracy of the simulated US data, even if only homogeneous displacements are simulated.

For heterogeneous displacement, the scheme proposed could effectively reduce the strain artefacts occurring when no correction was applied. For simulations performed at the limit of 4 PPWL (at maximum frequency), the results were accurate (error $<\sim$60 dB) within the specified range $[-c, e]$. These results are in agreement with the Fourier theory of US scattering and imply that accurate strain simulations can be performed if all spatial frequencies $\leq 2\cdot|\vec{k}_{wave}|$, are still sampled correctly after medium deformation. Moreover, this agreement with Fourier theory also implies that the lower bounds of the grid spacings in the sampling strategy proposed, Δx_{in} and Δx_{inter}, are limited by the Nyquist criterion only. The sampling strategy is therefore both accurate and computationally efficient. For simulations with a spacing Δx_{sim} smaller than the limit of 4 PPWL, accurate strain simulations are possible using the BLI even if no strain corrections are applied. The range of strains that can be simulated accurately without strain corrections increases with the number of PPWL used in the simulation. The sampling scheme with strain corrections, however, allows for accurate strain simulations with only 4 PPWL. It therefore allows for coarser simulation grids with reduced computation time, notably if large strains are simulated. It should be noted however, that the Fourier theory used neglects the influence of evanescent waves. Although the impact of evanescent waves on first-order echoes is small, higher-order scattering within several wavelengths may be influenced by the presence of evanescent waves [25]. Accurate simulation of higher-order scattering may therefore require a sampling of more than 4 PPWL. This requirement, however, depends on the medium and simulation method used and is not an intrinsic limitation of the sampling scheme proposed.

The sampling scheme was further compared with Field II, using a phantom with heterogeneous mechanical properties and a homogeneous speed of sound. Although the resulting strain results were very similar between the two methods, the Eulerian approach offers several advantages. First, the computation time in Lagrangian methods increases with the number of point scatterers present. In Eulerian methods, the computation time is relatively invariant with respect to the medium

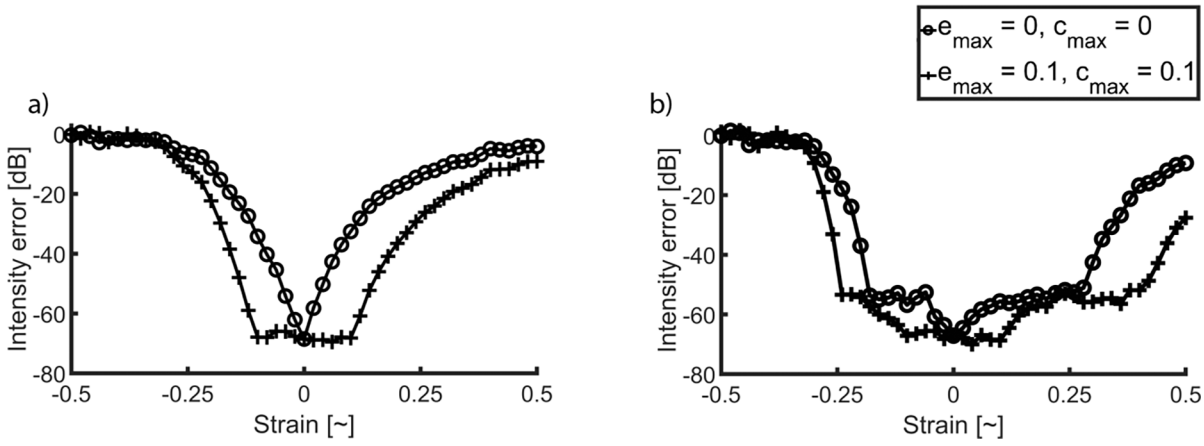

Fig. A1. The intensity error as function of applied strain to the speed of sound map is shown for the 37.5% and 75% bandwidth simulations in (a) and (b) respectively.

properties. For simulations of realistic speckle-rich *in vivo* images, the Eulerian approach is therefore less computationally demanding. Secondly, heterogeneities in the speed of sound, and higher-order scattering cannot be simulated in typical IRM-based Lagrangian methods [34], whereas these phenomena can be simulated in most Eulerian methods. However, for a fair comparison with Field II, higher-order scattering was not considered in this study by adding only small variations in acoustic properties to generate speckle. The ability to simulate strain imaging in media with heterogenous speed of sound was demonstrated using a simulation of a pulsating artery. The simulations of the artery in layered and aberrating speed of sound media showed expected behaviour, regarding image contrast and strain results. Another benefit of the Eulerian approach is the possibility to prescribe the acoustic properties on a grid, similar to ordinary images. This allows for the use of standard image processing software to define the acoustic properties maps and for straightforward comparisons with images from other modalities. Last, more complex physics, such as non-linear and elastic wave propagation, are typically simulated with Eulerian methods [17,35–37]. Although not investigated in this study, we hypothesize that strain simulations with non-linear and elastic wave propagation may be feasible with the sampling scheme proposed.

5. Conclusion

In this study, a sampling strategy to perform US strain simulations with Eulerian simulation methods was developed and validated. The method was validated using k-Wave simulations, in which point scatterers were displaced using both a Eulerian and a Lagrangian approach. A good agreement was found with respect to Fourier theory of US scattering. Furthermore, strain images obtained using k-Wave with the sampling scheme proposed were equivalent to those obtained using Field II for homogeneous media. The developed sampling strategy enables strain imaging simulations of media with heterogenous speed of sound distributions and higher-order scattering, using Eulerian simulation methods. The ability to simulate these phenomena is essential to increase the realism of simulated US images of *in vivo* tissue.

Declaration of Competing Interest

The authors declare that they have no known competing financial interests or personal relationships that could have appeared to influence the work reported in this paper.

Data availability

Data will be made available on request.

Acknowledgements

This research was funded by the Horizon 2020 Framework Programme (731771), and Stichting Lijf en Leven (37).

Appendix A

See Fig. A1.

References

[1] A. Ozturk, J.R. Grajo, M. Dhyani, B.W. Anthony, A.E. Samir, Principles of ultrasound elastography, Abdom. Radiol. (New York) 43 (2018) 773–785, https://doi.org/10.1007/s00261-018-1475-6.
[2] B.S. Garra, Elastography: history, principles, and technique comparison, Abdom. Imaging 40 (2015) 680–697, https://doi.org/10.1007/s00261-014-0305-8.
[3] R.M.S. Sigrist, J. Liau, A. El Kaffas, M.C. Chammas, J.K. Willmann, Ultrasound elastography: review of techniques and clinical applications, Theranostics 7 (2017) 1303–1329, https://doi.org/10.7150/thno.18650.
[4] N. Frulio, H. Trillaud, Ultrasound elastography in liver, Diagn. Interv. Imaging 94 (2013) 515–534, https://doi.org/10.1016/j.diii.2013.02.005.
[5] R.G. Barr, Shear wave liver elastography, Abdom. Radiol. 43 (2018) 800–807, https://doi.org/10.1007/s00261-017-1375-1.
[6] J.H. Youk, H.M. Gweon, E.J. Son, Shear-wave elastography in breast ultrasonography: the state of the art, Ultrasonography 36 (2017) 300–309, https://doi.org/10.14366/usg.17024.
[7] B. Liu, Y. Zheng, G. Huang, M. Lin, Q. Shan, Y. Lu, W. Tian, X. Xie, Breast lesions: quantitative diagnosis using ultrasound shear wave elastography—a systematic review and meta-analysis, Ultrasound Med. Biol. 42 (2016) 835–847, https://doi.org/10.1016/j.ultrasmedbio.2015.10.024.
[8] G.-Y. Li, Y. Cao, Mechanics of ultrasound elastography, Proc. Math. Phys. Eng. Sci. 473 (2017), 20160841, https://doi.org/10.1098/rspa.2016.0841.
[9] T. Varghese, Quasi-static ultrasound elastography, Ultrasound Clin. 4 (2009) 323–338, https://doi.org/10.1016/j.cult.2009.10.009.
[10] J.K. Dave, M.E. Mc Donald, P. Mehrotra, A.R. Kohut, J.R. Eisenbrey, F. Forsberg, Recent technological advancements in cardiac ultrasound imaging, Ultrasonics 84 (2018) 329–340, https://doi.org/10.1016/j.ultras.2017.11.013.
[11] M. Couade, The advent of ultrafast ultrasound in vascular imaging: a review, J. Vasc. Diagnostics Interv. (2016) 9–22, https://doi.org/10.2147/jvd.s68045.
[12] M. Cikes, L. Tong, G.R. Sutherland, J. D'hooge, Ultrafast cardiac ultrasound imaging: technical principles, applications, and clinical benefits, JACC Cardiovasc. Imaging 7 (2014) 812–823, https://doi.org/10.1016/j.jcmg.2014.06.004.
[13] S. Cournane, A.J. Fagan, J.E. Browne, Review of ultrasound elastography quality control and training test phantoms, Ultrasound 20 (2012) 16–23, https://doi.org/10.1258/ult.2011.011033.
[14] A. Swillens, G. De Santis, J. Degroote, L. Lovstakken, J. Vierendeels, P. Segers, Accuracy of carotid strain estimates from ultrasonic wall tracking: a study based on multiphysics simulations and in vivo data, IEEE Trans. Med. Imaging 31 (2012) 131–139, https://doi.org/10.1109/TMI.2011.2165959.
[15] S. Park, S.R. Aglyamov, W.G. Scott, S.Y. Emelianov, Strain imaging using conventional and ultrafast ultrasound imaging: numerical analysis, IEEE Trans. Ultrason. Ferroelectr. Freq. Control. 54 (2007) 987–995, https://doi.org/10.1109/TUFFC.2007.344.
[16] H. Li, Y. Guo, W.-N. Lee, Systematic performance evaluation of a cross-correlation-based ultrasound strain imaging method, Ultrasound Med. Biol. 42 (2016) 2436–2456, https://doi.org/10.1016/j.ultrasmedbio.2016.06.015.

[17] M.D. Verweij, B.E. Treeby, K.W.A. van Dongen, L. Demi, 2.19 - Simulation of ultrasound fields, in: A. Brahme (Ed.), Compr. Biomed. Phys., Elsevier, Oxford, 2014, pp. 465–500, https://doi.org/10.1016/B978-0-444-53632-7.00221-5.
[18] H. Gao, T. Hergum, H. Torp, J. D'hooge, Comparison of the performance of different tools for fast simulation of ultrasound data, Ultrasonics 52 (2012) 573–577, https://doi.org/10.1016/j.ultras.2012.01.009.
[19] M. Makūnaitė, R. Jurkonis, A. Lukoševičius, M. Baranauskas, Main uncertainties in the RF ultrasound scanning simulation of the standard ultrasound phantoms, Sensors 21 (13) (2021), 4420, https://doi.org/10.3390/s21134420.
[20] R.J. McGough, Rapid calculations of time-harmonic nearfield pressures produced by rectangular pistons, J. Acoust. Soc. Am. 115 (2004) 1934–1941, https://doi.org/10.1121/1.1694991.
[21] J. Gu, Y. Jing, mSOUND: an open source toolbox for modeling acoustic wave propagation in heterogeneous media, IEEE Trans. Ultrason. Ferroelectr. Freq. Control. 68 (2021) 1476–1486, https://doi.org/10.1109/TUFFC.2021.3051729.
[22] B.E. Treeby, B.T. Cox, k-Wave: MATLAB toolbox for the simulation and reconstruction of photoacoustic wave fields, J. Biomed. Opt. 15 (2010) 21314, https://doi.org/10.1117/1.3360308.
[23] J.A. Jensen, A model for the propagation and scattering of ultrasound in tissue, J. Acoust. Soc. Am. 89 (1991) 182–190, https://doi.org/10.1121/1.400497.
[24] A.J. Devaney, A filtered backpropagation algorithm for diffraction tomography, Ultrason Imaging 4 (1982) 336–350, https://doi.org/10.1016/0161-7346(82)90017-7.
[25] M.F. Schiffner, G. Schmitz, Plane wave pulse-echo ultrasound diffraction tomography with a fixed linear transducer array, in: A. Nowicki, J. Litniewski, T. Kujawska (Eds.), Acoust. Imaging, Springer, Netherlands, Dordrecht, 2012, pp. 19–30, https://doi.org/10.1007/978-94-007-2619-2_3.
[26] E.S. Wise, B.T. Cox, J. Jaros, B.E. Treeby, Representing arbitrary acoustic source and sensor distributions in Fourier collocation methods, J. Acoust. Soc. Am. 146 (2019) 278–288, https://doi.org/10.1121/1.5116132.
[27] J.-W. Muller, M.U. Arabul, H.-M. Schwab, M.C.M. Rutten, M.R.H.M. van Sambeek, M. Wu, R.G.P. Lopata, Modeling toolchain for realistic simulation of photoacoustic data acquisition, J. Biomed. Opt. 27 (2022), 96005, https://doi.org/10.1117/1.JBO.27.9.096005.
[28] A.H. Barnett, J. Magland, L. af Klinteberg, A parallel nonuniform fast Fourier transform library based on an "Exponential of Semicircle" kernel, SIAM J. Sci. Comput. 41 (2019) C479–C504, https://doi.org/10.1137/18M120885X.
[29] K. Farahani, R. Naghdabadi, Conjugate stresses of the Seth-Hill strain tensors, Int. J. Solids Struct. 37 (2000) 5247–5255, https://doi.org/10.1016/S0020-7683(99)00209-7.
[30] J.A. Jensen, N.B. Svendsen, Calculation of pressure fields from arbitrarily shaped, apodized, and excited ultrasound transducers, IEEE Trans. Ultrason. Ferroelectr. Freq. Control. 39 (1992) 262–267, https://doi.org/10.1109/58.139123.
[31] J.R. Shewchuk, Triangle: engineering a 2D quality mesh generator and Delaunay triangulator, in: M.C. Lin, D. Manocha (Eds.), Appl. Comput. Geom. Towar. Geom. Eng, Springer Berlin, Heidelberg, Berlin, Heidelberg, 1996, pp. 203–222, https://doi.org/10.1007/BFb0014497.
[32] R.G.P. Lopata, H.H.G. Hansen, M.M. Nillesen, J.M. Thijssen, C.L. De Korte, Comparison of one-dimensional and two-dimensional least-squares strain estimators for phased array displacement data, Ultrason Imaging 31 (2009) 1–16, https://doi.org/10.1177/016173460903100101.
[33] C.L. de Korte, E.I. Céspedes, A.F.W. van der Steen, C.T. Lancée, Intravascular elasticity imaging using ultrasound: feasibility studies in phantoms, Ultrasound Med. Biol. 23 (1997) 735–746, https://doi.org/10.1016/S0301-5629(97)00004-5.
[34] A. Cigier, F. Varray, D. Garcia, SIMUS: an open-source simulator for medical ultrasound imaging. Part II: comparison with four simulators, Comput. Methods Programs Biomed. 220 (2022), 106774, https://doi.org/10.1016/j.cmpb.2022.106774.
[35] B.E. Treeby, J. Jaros, D. Rohrbach, B.T. Cox, Modelling elastic wave propagation using the k-Wave MATLAB Toolbox, in: 2014 IEEE Int, Ultrason. Symp. (2014) 146–149, https://doi.org/10.1109/ULTSYM.2014.0037.
[36] M. Verweij, L. Demi, K.W.A. van Dongen, Computation of nonlinear ultrasound fields using a linearized contrast source method, J. Acoust. Soc. Am. 134 (2013) 1442–1453, https://doi.org/10.1121/1.4812863.
[37] K. Wang, E. Teoh, J. Jaros, B.E. Treeby, Modelling nonlinear ultrasound propagation in absorbing media using the k-Wave toolbox: experimental validation, in: 2012 IEEE Int, Ultrason. Symp. (2012) 523–526, https://doi.org/10.1109/ULTSYM.2012.0130.